Nano Research

Open Access

Research Article

Ultrafast electrochemical selenium doping strategy and the role of selenium in nickel-cobalt sulfide for enhanced overall water splitting

Guojing Wang[1,2,§], Yuzhuo Sun[1,§], Yidan Zhao[1], Chen Deng[3], Yuanzhi Zhu[2]✉, and Yunchao Li[1]✉

[1] *Key laboratory of Theoretical and Computational Photochemistry, Ministry of Education, College of Chemistry, Beijing Normal University, Beijing 100875, China*
[2] *Faculty of Chemical Engineering, Yunnan Provincial Key Laboratory of Energy Saving in Phosphorus Chemical Engineering and New Phosphorus Materials, Kunming University of Science and Technology, Kunming 650500, China*
[3] *PetroChina Shenzhen New Energy Research Institute Co., Ltd., Shenzhen 518052, China*
[§] *Guojing Wang and Yuzhuo Sun contributed equally to this work.*

Cite this article: *Nano Research*, **2025**, *18*, 94907165. https://doi.org/10.26599/NR.2025.94907165

ABSTRACT: Heteroatom doping has emerged as an effective strategy to enhance the performance of electrocatalysts for hydrogen evolution reaction (HER) and oxygen evolution reaction (OER). Traditional doping methods often involve harsh chemical treatments and tedious procedures, hindering their widespread applications. Furthermore, although dynamic surface reconstruction in alkaline media is commonly observed in bimetallic compounds, strategies to regulate this reconstruction behavior for enhanced HER and OER performances remain inadequately explored. Herein, we report an ultrafast (≤ 300 s) and mild electrochemical doping approach to fabricate Se-doped $NiCo_2S_4$ hollow nanoarrays on carbon fiber papers (*a*-$NiCo_2(S_{1-x}Se_x)_4$), investigating the role of Se in enhancing overall water splitting performance. Under HER conditions, *a*-$NiCo_2(S_{1-x}Se_x)_4$ demonstrates remarkable stability, with Se tuning the electronic structure to optimize intermediate adsorption and facilitate H_2O dissociation. While under OER conditions, Se doping lowers the energy barrier for reconstruction and promotes transformation into active Se, S co-doped $Ni_{0.33}Co_{0.67}OOH$ nanosheets. The optimal samples exhibit superior HER and OER activity, requiring a cell voltage of 1.578 V to deliver a current density of 100 mA·cm^{-2} for overall water splitting. This work not only introduces a facile method for Se doping but also provides comprehensive insights into the structure–composition–activity relationship for Se-doped bimetallic sulfide.

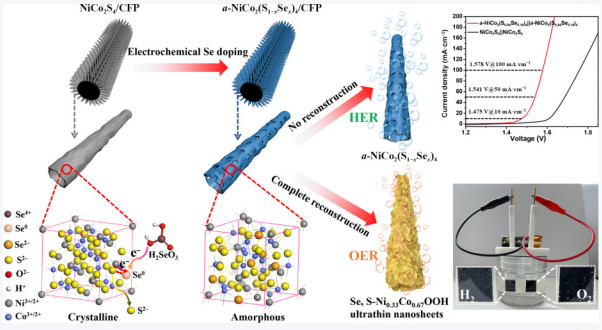

KEYWORDS: electrochemical Se doping, amorphous $NiCo_2(S_{1-x}Se_x)_4$ porous nanoarrays, electrochemical reconstruction, electronic structure modulation, overall water splitting

1 Introduction

Hydrogen production through electrochemical water splitting represents a promising avenue for a sustainable and eco-friendly global energy supply [1–3]. However, the electrocatalytic water splitting is severely restricted by the large overpotentials and sluggish kinetics associated with the cathodic hydrogen evolution reaction (HER) and anodic oxygen evolution reaction (OER) [4–7]. Non-noble metal-based materials, such as transition metal oxides, hydroxides, phosphides, selenides and sulfides, are recognized as efficient and low-cost electrocatalysts for water splitting [8–12]. During redox electrolysis, theses catalysts commonly undergo reconstruction to a certain extent, leading to new active centers with enhanced stability [13, 14]. However, the majority of these electrocatalysts are exclusively limited to catalyzing either the HER or the OER.

In order to reduce the synthesis and maintanence cost and avoid the cross-contamination between the two electrodes, efforts have focused on developing single-component bifunctional catalysts that can effectively catalyze both reactions [15, 16]. Bimetallic sulfides, such as $NiCo_2S_4$, have emerged as representative bifunctional electrocatalysis in overall water splitting, attributed to their hybridized d orbitals and versatile redox properties [17–19]. For instance, Li et al. reported the N-doped carbon coated $NiCo_2S_4$

Received: September 24, 2024; **Revised:** November 30, 2024
Accepted: December 2, 2024

✉Address correspondence to Yunchao Li, liyc@bnu.edu.cn; Yuanzhi Zhu, yuanzhi_zhu@kust.edu.cn

hollow nanotube, exhibiting low overpotentials of 295 and 330 mV for HER and OER to afford 100 mA·cm^{-2} in 1.0 M KOH, respectively [20]. Sivanantham et al. reported an $NiCo_2S_4$ nanowire arrays on an Ni foam as a bifunctional catalyst and acquired a low cell voltage of 1.56 V at a current density of 10 mA·cm^{-2} for overall water splitting [21]. Nonetheless, further engineering the electronic structure and the reconstruction behavior of $NiCo_2S_4$ for enhanced electrocatalytic performance remains in its early stages.

Heteroatom doping has emerged as a highly effective strategy to enhance the performance of transition metal-based electrocatalysts [22–24]. Compared with common P and S doping strategies, Se doping is less conventional but may be more effective for improving the performance of transition metal-based electrocatalysis. In contrast to P and S, Se offers a broader range of oxidation states and more stable intermediate oxidation states [25], facilitating a more comprehensive modulation of the electronic structure. Additionally, with its larger covalent radius, Se forms weaker metal–Se bonds than P and S, leading to easier bond breaking upon reactions [25]. This characteristic promotes the complete structural reconstruction of the Se-contained materials, thereby enhancing their activity and stability. For example, Se doping could modulate the electronic structure of P vacancies in NiP_2 and CoS_2, leading to enhanced HER performance [26, 27]. The FeSe pre-catalyst undergone complete self-reconstruction into Se-doped FeOOH during OER, resulting in improved OER activity [28]. However, traditional doping methods frequently involve high-temperature, hydrothermal or complex synthesis procedures, thus hindering the doping efficiency [29–32]. Furthermore, although dynamic surface reconstruction in alkaline media is commonly observed in bimetallic compounds, comprehensive investigations into the activity origins and structural reconstruction of bifunctional bimetallic sulfides for water splitting remain unexplored.

Herein, we report a rapid, mild and controllable electrochemical anion doping approach to fabricate amorphous porous Se-doped nickel-cobalt sulfide hollow nanorod arrays on carbon fiber paper (*a*-$NiCo_2(S_{1-x}Se_x)_4$/CFP). This approach allows for the adjustment of the Se doping content across a broad range while preserving the pristine structure of $NiCo_2S_4$ nanoarrays. Consequently, it enables a systematic exploration of the effects of Se doping on the electronic structure and reconstruction behavior of $NiCo_2S_4$. Under HER conditions, the *a*-$NiCo_2(S_{1-x}Se_x)_4$/CFP demonstrates remarkable stability, with Se tuning the electronic structure to optimize intermediate adsorption and facilitate H_2O dissociation. For OER conditions, Se doping lowers the energy barrier for reconstruction and promotes phase transformation into highly active Se, S co-doped $Ni_{0.33}Co_{0.67}OOH$ ultrathin nanosheets. The optimal samples exhibit ultrahigh electrocatalytic activity and outstanding durability, delivering a current density of 100 mA·cm^{-2} at overpotentials of 98 mV for HER, 215 mV for OER and 348 mV for overall water splitting, respectively. This work not only introduces a facile method for Se doping but also provides comprehensive insights into the structure–composition–activity relationship for Se-doped bimetallic sulfide.

2 Experimental

2.1 Synthesis of $NiCo_2(CO_3)_{1.5}(OH)_3$

Typically, $Co(NO_3)_2{\cdot}6H_2O$ (0.349 g, 1.2 mmol), $Ni(NO_3)_2{\cdot}6H_2O$ (0.174 g, 0.6 mmol) and urea (0.360 g, 6 mmol) were dissolved in 40 mL deionized (DI) water under magnetic stirring for 30 min to prepare the precursor solution. Then, the as-obtained solution and a piece of pretreated CFP (1 cm × 3 cm) were loaded into a 50 mL Teflon-lined stainless steel autoclave and then the autoclave was sealed and kept at 120 °C for 10 h and subsequently cooled to room temperature naturally. Then, the CFP coated with the $NiCo_2(CO_3)_{1.5}(OH)_3$ nanoneedle arrays was isolated and then washed with water and ethanol three times to purify the product. Next, the product was dried at 60 °C for 12 h under vacuum.

2.2 Synthesis of $NiCo_2S_4$

$NiCo_2S_4$ electrode was synthesized by a sulfidization process. First, typically, the as-obtained $NiCo_2(CO_3)_{1.5}(OH)_3$ was added into 30 mL of aqueous solution containing 300 mg of thioacetamide and then the mixture was transferred into an autoclave and heated at 140 °C for 5 h. After cooling down to room temperature naturally, the electrode was washed with deionized water and ethanol for three times, respectively and then dried under vacuum at 60 °C for 12 h.

2.3 Synthesis of $NiCo_2Se_4$

$NiCo_2Se_4$ electrode was synthesized by a selenization process. A piece of the $NiCo_2(CO_3)_{1.5}(OH)_3$, 24 mL of water and the as-prepared NaHSe solution (approximately 1 mL) were placed in a 50 mL Teflon-lined stainless steel autoclave. The solution in the autoclave was purged with argon gas for 1 h and then sealed and maintained at 120 °C for 20 h. The resulting $NiCo_2Se_4$ electrode was separated, the electrode was washed with deionized water and ethanol for three times, respectively and then dried at 60 °C for 12 h under vacuum.

2.4 Synthesis of *a*-$NiCo_2(S_{1-x}Se_x)_4$

All electrochemical doping experiments were carried out on an IVIUM electrochemical workstation (Netherlands) with a three-electrode setup consisting of an Ag/AgCl (saturated KCl) reference electrode, glassy carbon (GC) as the counter electrode and $NiCo_2S_4$ (1 cm × 1 cm) as the working electrode. the electrolyte solution used for deposition contained 10 mM SeO_2 and 25 mM $(NH_4)_2SO_4$ dissolved in water was freshly prepared and purged with N_2 for 30 min before electrochemical doping. All electrochemical doping experiments were carried out at room temperature in acidic solution (pH 2.8) on $NiCo_2S_4$ (1 cm × 1 cm) at an applied potential of −0.8 V vs. Ag/AgCl for different time (100, 300 and 600 s). The resulting electrodes were carefully washed several times with DI water to remove surface ions and then dried in dried at 60 °C under vacuum for 12 h. Then, the *a*-$NiCo_2(S_{1-x}Se_x)_4$ was obtained, where x is equivalent to different Se/(S + Se) ratios (x = 0.08, 0.16, or 0.28) from inductively coupled plasma-mass spectrometry (ICP-MS) analysis. The mass loadings of various *a*-$NiCo_2(S_{1-x}Se_x)_4$ on CFP were determined to be ca. 3 mg/cm^2 based on weighing.

2.5 Electrochemical measurements

All electrochemical measurements were performed using an IVIUM electrochemical workstation (Netherlands) using a conventional three-electrode cell in H_2 or O_2-saturated 1.0 M KOH electrolyte. The as-prepared electrodes, Ag/AgCl (KCl saturated) and graphite rod (for HER) or Pt wire (for OER) were used as working electrode (1 cm^2 electrode area), reference electrode and counter electrode, respectively. In the HER and OER test, all the

electrodes were cycled 20 times by cyclic voltammetry (CV) for the activation prior to measuring each polarization curve. Linear scan voltammetry (LSV) and CV curves were recorded in a supporting electrolyte at a scan rate of 5 mV·s^{-1}. All electrochemical impedance spectroscopy (EIS) measurements were carried out by sampling 100 points in the frequency range from 100 kHz to 0.01 Hz with an alternating current (AC) perturbation of 5 mV at ambient temperature. A chronopotentiometry (CP) experiment at a constant current density of 100 mA·cm^{-2} and LSV before and after 10,000 CV cycles were performed for durability testing. All plots for evaluating the electrocatalytic activity toward the HER or OER were corrected by a background capacitive current and ohmic potential drop (*iR*) based on the series resistances derived from EIS. For the overall water splitting test, two symmetric catalyst electrodes were used as the anode and cathode.

2.6 Computational methods

Density functional theory (DFT) calculations were conducted using Vienna *ab initio* simulation package (VASP) [33, 34], using the projector-augmented wave (PAW) method to describe the interaction between ionic cores and valence electrons [35]. The generalized gradient approximation (GGA) with the Perdew–Burke–Ernzerhof (PBE) functional was selected to compute electron exchange and correlation energies [36, 37]. The cut-off energies for plane wave expansions were set to 400 eV. The Brillouin zone of the systems was sampled using 2 × 2 × 2 Gama *k*-point grids for geometric optimization of the slab surface cells. In the structural optimization, the two topmost surface layers were allowed to fully relax until the residual force per atom was less than 0.02 eV·Å^{-1} and the energy convergence threshold was set to 10^{-5} eV. For the HER process, the (311) surface facets of $NiCo_2S_4$ and Se-$NiCo_2S_4$ were modeled by p (2 × 2) supercell slabs with six atomic layers. Gibbs free energy change (ΔG) of chemical reaction was calculated by the following equation $\Delta G = \Delta E + \Delta ZPE - T\Delta S$, where E, ZPE, T and S denote the calculated total energy, zero-point energy, temperature and entropy, respectively [38]. H_2O and intermediates (OH and H) are first adsorbed on all possible active sites of the slab surfaces. The climbing image-nudged elastic band (CI-NEB) method was then used to locate the transition states for H_2O dissociation. All transition states were verified via vibration analyses with only one imaginary frequency. For the OER process, $Ni_{0.33}Co_{0.67}OOH$ (001), S-$Ni_{0.33}Co_{0.67}OOH$ (001) and S, Se-$Ni_{0.33}Co_{0.67}OOH$ (001) were modeled by p (2 × 2) supercell slabs with nine atomic layers, respectively. the conventional four-step mechanism (*OH, *O, *OOH and *O_2; * denotes the active site) was adopted to describe the OER process. The Gibbs free energy diagrams were estimated by the following equation $\Delta G_i = \Delta E_i + \Delta ZPE_i - T\Delta S_i - eU$, where i represents *OH, *O, or *OOH intermediates, U is the potential against normal hydrogen electrode (NHE) at standard conditions and e is the transferred charge [39]. A vacuum spacing of 15 Å was used to avoid the interaction between the slabs and dipole correction was also included to eliminate the spurious contributions arising from the asymmetry of the system along the z direction. All calculations are spin polarized.

The d-band or p-band center was calculated by using the following equation

$$\varepsilon_{d/p} = \int n_{d/p}(\varepsilon)\,\varepsilon d\varepsilon \Big/ \int n_{d/p}(\varepsilon)\,d\varepsilon$$

where $\varepsilon_{d/p}$ is the d-band or p-band center, $n_{d/p}(\varepsilon)$ is the density of states (DOS) and ε is the bonding energy.

3 Results and discussion

3.1 Electrochemical Se doping and structural characterizations

The three-step synthetic process of *a*-$NiCo_2(S_{1-x}Se_x)_4$ is illustrated in Fig. 1(a). To more accurately reflect the intrinsic activity of the catalyst, CFP (scanning electron microscopy (SEM) and X-ray diffraction (XRD) in Fig. S1 in the Electronic Supplementary Material (ESM)) instead of Ni foam was selected as the substrate for catalyst growth. The $NiCo_2(CO_3)_{1.5}(OH)_3$ nanoneedles were directly grown on the CFP through hydrothermal method, which subsequently transformed into $NiCo_2S_4$ hollow nanorods through hydrothermal sulfurization. The $NiCo_2S_4$ nanoarrays were then converted into amorphous porous *a*-$NiCo_2(S_{1-x}Se_x)_4$ via electrochemical reduction doping process in aqueous solution of SeO_2 and $(NH_4)_2SO_4$. Figure 1(b) illustrates the reaction mechanism of electrochemical doping. The SeO_2 reacts with water to form H_2SeO_3 (a weak binary acid, reaction 1), which undergoes reduction reaction at the cathode to produce elemental Se (reaction 2). The production of Se element can be demonstrated by the presence of a large amount of reddish-brown material on and near the working electrode (Fig. S2 in the ESM). The $(NH_4)_2SO_4$ serves as the pH buffer to provide an acidic environment. The metal sulfides exhibit unique adsorption and reaction properties for Se and SeO_3^{2-} through surface complexation and ionic exchange (reaction 3) [40], which is further enhanced under the applied reduction potential (−0.8 V vs. Ag/AgCl). Interestingly, under this reduction potential, no HER was observed on the electrode surface, suggesting a faster reaction kinetics of selenization reaction than HER.

$$SeO_2 + H_2O \rightarrow H_2SeO_3 \quad (1)$$

$$H_2SeO_3 + 4e^- + 4H^+ \rightarrow Se + 3H_2O \quad (2)$$

$$4xSe + 8xe^- + NiCo_2S_4 \rightarrow NiCo_2(S_{1-x}Se_x)_4 + 4xS^{2-} \quad (3)$$

The morphological and structural analyses were further performed using SEM, transmission electron microscopy (TEM) and XRD. Figure S3 in the ESM (SEM, TEM and XRD) display that the vertically aligned $NiCo_2(CO_3)_{1.5}(OH)_3$ nanoneedles with an average diameter of ~ 100 nm are uniformly covered on CFP. Driven by the Kirkendall effect and release of H_2S, the sulfurization process results in hollow $NiCo_2S_4$ nanorods with a rough surface (Figs. 2(a) and 2(b)) while maintaining overall structural integrity (SEM in Fig. S4(a) in the ESM). The high-resolution TEM (HRTEM) imaging and selected area electron diffraction (SAED) analysis (Fig. 2(c)) reveal continuous square lattice fringes and discrete diffraction spots, confirming the crystalline nature of $NiCo_2S_4$. The interplanar spacings are measured to be 2.344 and 2.822 Å, corresponding to the (400) and (311) planes of the cubic $NiCo_2S_4$ phase.

The SEM (Fig. 2(d) and Fig. S4(b) in the ESM) and TEM images (Fig. 2(e)) of *a*-$NiCo_2(S_{1-x}Se_x)_4$ show that the electrochemical Se doping process create a porous structure on the nanorods. No obvious lattice fringes were observed on the HRTEM image of *a*-

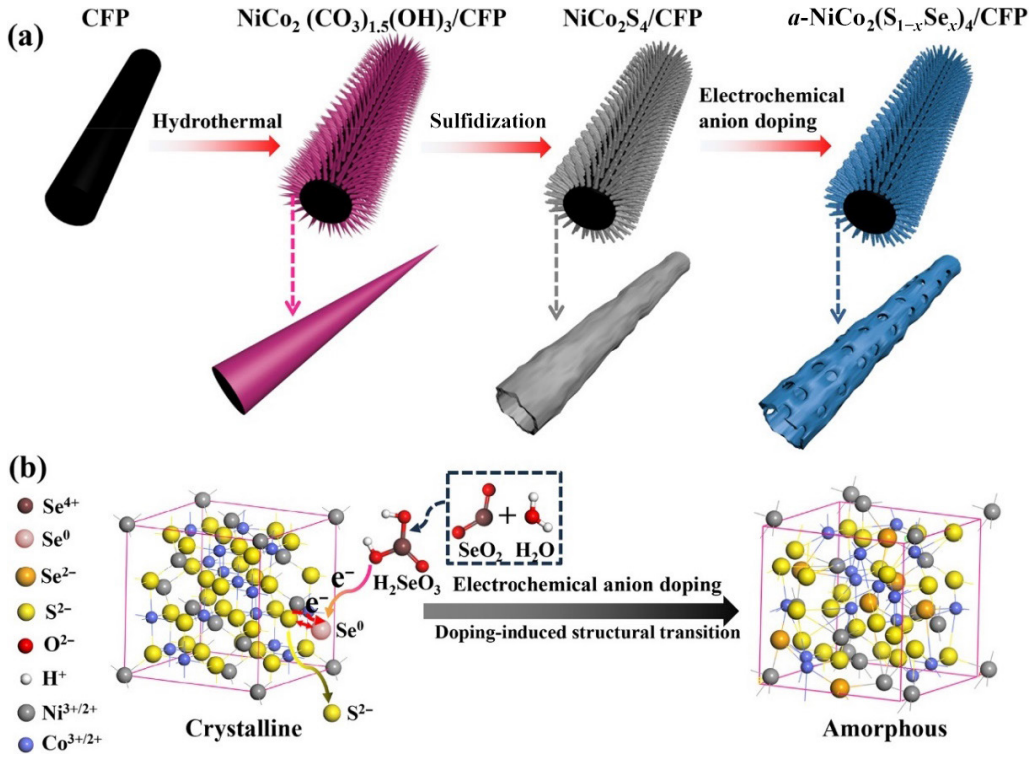

Figure 1 Schematic illustration of (a) the fabricating process and (b) the formation mechanisms of a-$NiCo_2(S_{1-x}Se_x)_4$.

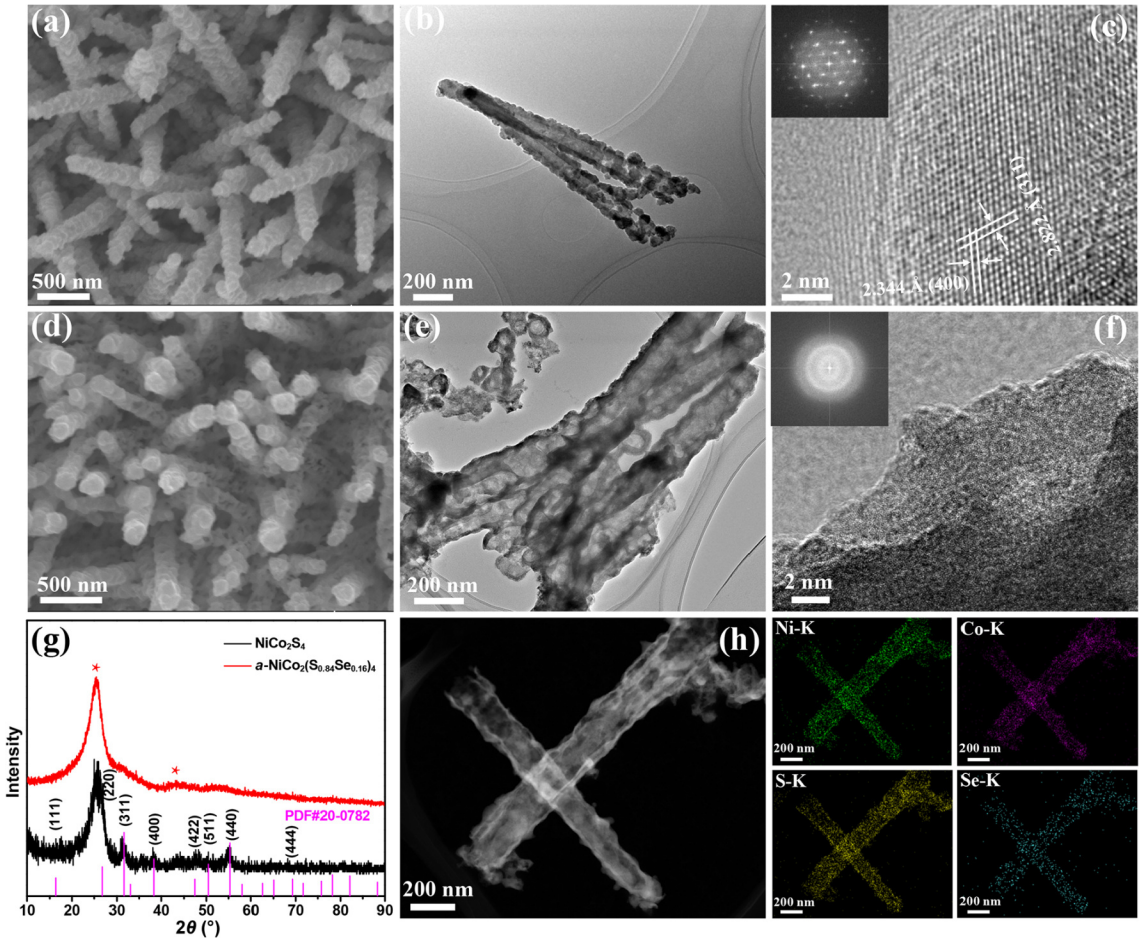

Figure 2 (a) and (d) SEM, (b) and (e) TEM and (c) and (f) HRTEM images of ((a)–(c)) $NiCo_2S_4$ and ((d)–(f)) a-$NiCo_2(S_{0.84}Se_{0.16})_4$; the inset of (c) and (f) is the corresponding SAED pattern. (g) XRD patterns of $NiCo_2S_4$ and a-$NiCo_2(S_{0.84}Se_{0.16})_4$ and (h) elemental mapping of a-$NiCo_2(S_{0.84}Se_{0.16})_4$.

$NiCo_2(S_{1-x}Se_x)_4$, consistent with the SAED analysis (Fig. 2(f)). The XRD patterns further confirm that the selenium doping converts crystalline $NiCo_2S_4$ into an amorphous structure, with the absence of diffraction peaks other than CFP signals (Fig. 2(g)). In addition, the high angle annular dark-field scanning TEM (HAADF-STEM) and element mapping images in Fig. 2(h) provide clear visual evidences that the Ni, Co, S and Se elements are homogeneously distributed on *a*-$NiCo_2(S_{1-x}Se_x)_4$. Moreover, the energy-dispersive X-ray (EDX) spectroscopy spectrum (Fig. S5 in the ESM) and ICP-atomic emission spectrometry (ICP-AES) analyses consistently reveal an average Ni/Co/S/Se atomic ratio as 1:2:3.34:0.66, corresponding to *a*-$NiCo_2(S_{0.84}Se_{0.16})_4$. Notably, the Se/S ratios can be tuned by altering the electrochemical doping time (Table S1 in the ESM). As a conceptual proof, we further synthesized the *a*-$NiCo_2(S_{0.92}Se_{0.08})_4$ and *a*-$NiCo_2(S_{0.72}Se_{0.28})_4$ and their SEM, TEM and EDX characterization results are given in Fig. S6 in the ESM. Interestingly, all samples display an amorphous structure, with porosity incrementally increasing alongside the degree of Se doping. Despite this, the total atomic ratio of S and Se consistently maintains at 4, indicating a substitutional doping mechanism. The larger atomic radius of Se introduces lattice strain and mismatches, leading to strain release in hollow nanorods, which accounts for such local structural dissociation and pore formation.

The surface chemical state and composition of the $NiCo_2S_4$ and *a*-$NiCo_2(S_{0.84}Se_{0.16})_4$ are analyzed by X-ray photoelectron spectroscopy (XPS) (Figs. 3(a)–3(d)). The Ni 2p spectra of pristine $NiCo_2S_4$ (Fig. 3(a)) can be deconvoluted into Ni^{2+} (853.4 eV) and Ni^{3+} (854.6 eV) for Ni $2p_{3/2}$, as well as Ni^{2+} (870.5 eV) and Ni^{3+} (872.4 eV) for Ni $2p_{1/2}$, respectively. In the Co 2p spectra (Fig. 3(b)), peaks at 778.8 and 779.6 eV correspond to Co^{3+} and Co^{2+} in the $2p_{3/2}$ region, while peaks at 793.7 and 795.1 eV are assigned to Co^{3+} and Co^{2+} in the $2p_{1/2}$ region, respectively. The S 2p of $NiCo_2S_4$ (Fig. 3(c)) can be deconvoluted into a pair of peaks located at around 162.3 and 163.6 eV, assigned to the metal–S bonds for S $2p_{3/2}$ and S $2p_{1/2}$, respectively. These results are consistent with previously reported XPS results for $NiCo_2S_4$ [41–43]. After Se doping, a distinct Se XPS signal is observed for *a*-$NiCo_2(S_{0.84}Se_{0.16})_4$ (Fig. 3(d)), which can be deconvoluted into $3d_{5/2}$ and $3d_{3/2}$ doublets for metal–Se bonds, accompanied by a small peak at 60.4 eV associated with SeO_x species [44]. It should be noted that the Ni 2p, Co 2p and S 2p peaks of *a*-$NiCo_2(S_{0.84}Se_{0.16})_4$ exhibit an obvious negative shift (0.3–0.5 eV) compared with those of $NiCo_2S_4$. This suggests a notable increase in electron density around the Ni, Co, S atoms, attributed to the weaker electronegativity and higher electron-donating capacity of Se than S.

X-ray absorption spectroscopy (XAS) was employed to further investigate the electronic and local geometrical structures of these samples. The Ni K-edge X-ray absorption near-edge structure (XANES) spectra (Fig. 4(a)) reveal significant deviations from standard Ni foil and NiO references for both $NiCo_2S_4$ and *a*-$NiCo_2(S_{0.84}Se_{0.16})_4$, indicating distinct chemical environments for these samples. Compared with $NiCo_2S_4$, $NiCo_2(S_{0.84}Se_{0.16})_4$ shows a noticeable shift of ~ 0.2 eV towards lower energy at the rising-edge region (the inset of Fig. 4(a)), which suggests a decrease in Ni's oxidation state in *a*-$NiCo_2(S_{0.84}Se_{0.16})_4$, in agreement with the XPS results. The Fourier-transformed (FT) extended X-ray absorption fine structure (EXAFS) spectra of Ni K-edge show similar peak profiles for *a*-$NiCo_2(S_{0.84}Se_{0.16})_4$ and $NiCo_2S_4$, suggesting similar bonding parameters of Ni in both samples (Fig. 4(b)). Furthermore, the FT-EXAFS spectra were carefully fitted to determine their

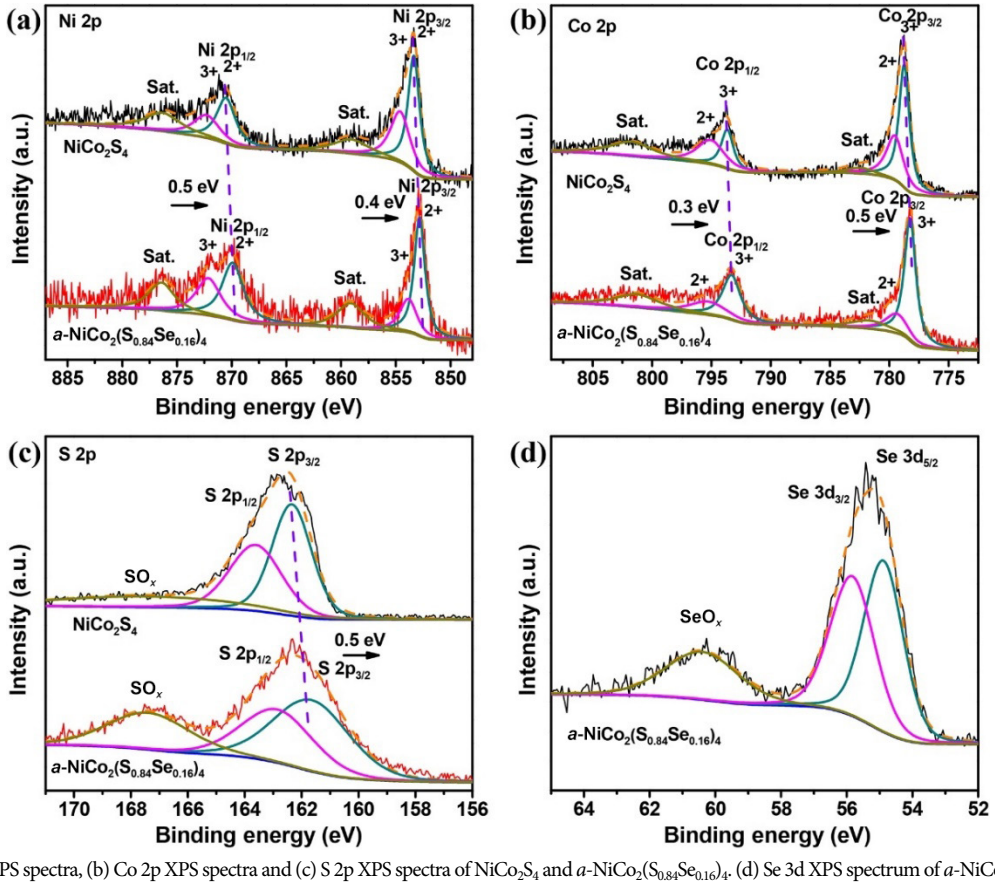

Figure 3 (a) Ni 2p XPS spectra, (b) Co 2p XPS spectra and (c) S 2p XPS spectra of $NiCo_2S_4$ and *a*-$NiCo_2(S_{0.84}Se_{0.16})_4$. (d) Se 3d XPS spectrum of *a*-$NiCo_2(S_{0.84}Se_{0.16})_4$.

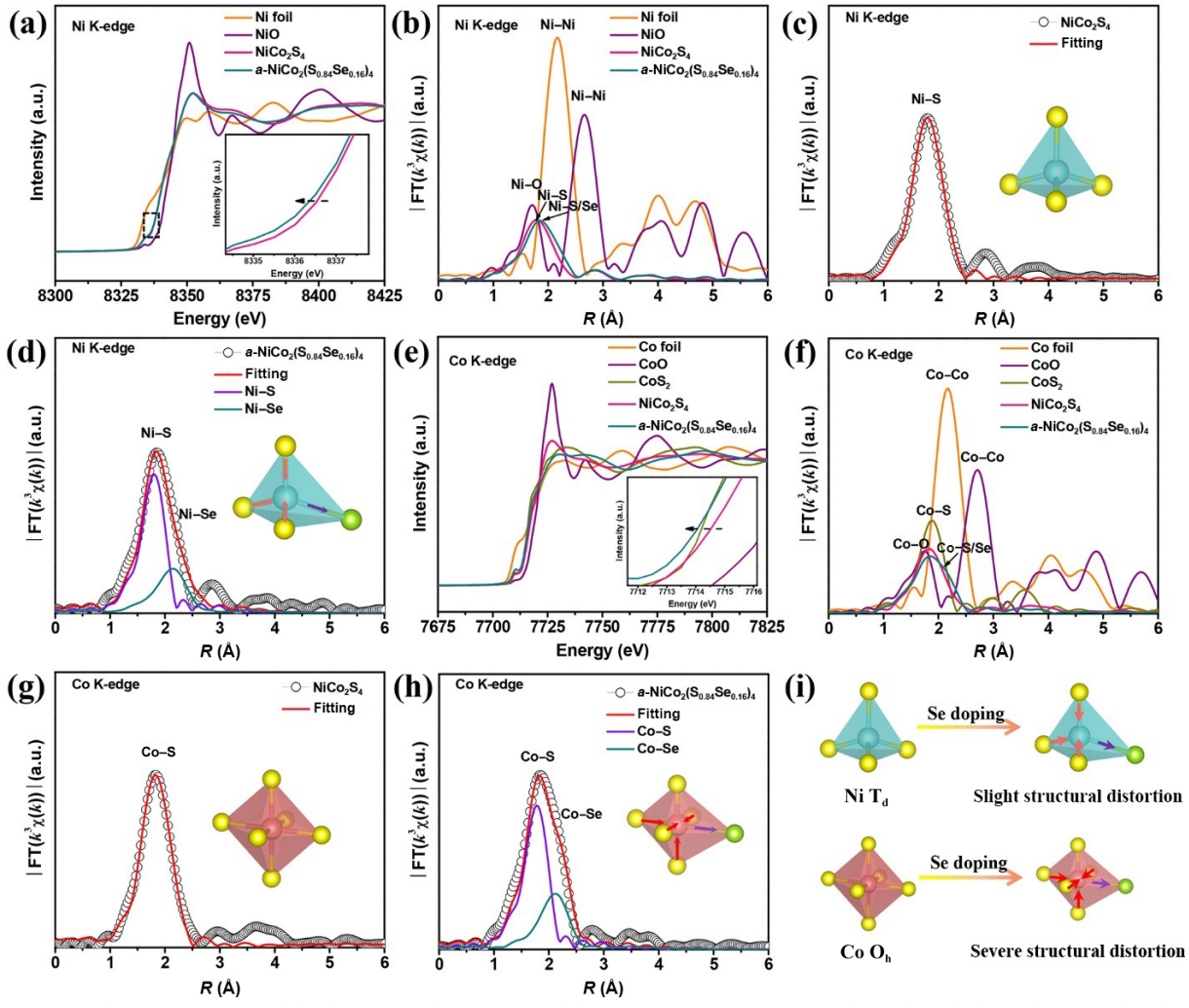

Figure 4 (a) Ni K-edge XANES spectra and (b) the corresponding FT curves of the $NiCo_2S_4$, *a*-$NiCo_2(S_{0.84}Se_{0.16})_4$, Ni foil and standard NiO, the inset is the enlarged view of the pre-edge profiles. EXAFS fitting in *R* space at the Ni K-edge of (c) $NiCo_2S_4$ and (d) *a*-$NiCo_2(S_{0.84}Se_{0.16})_4$. (e) Co K-edge XANES spectra and (f) the corresponding FT curves of the $NiCo_2S_4$, *a*-$NiCo_2(S_{0.84}Se_{0.16})_4$, CoS_2, Co foil and standard CoO, the inset is the enlarged view of the pre-edge profiles. EXAFS fitting in *R* space at the Co K-edge of (g) $NiCo_2S_4$ and (h) *a*-$NiCo_2(S_{0.84}Se_{0.16})_4$. (i) Schematic diagram of Se doping induced structural distortion of Ni T_d (T_d: tetrahedron) and Co O_h (O_h: octahedral).

structural parameters (Figs. 4(c) and 4(d) and Table S2 in the ESM). Due to the weaker Ni–Se interaction compared with Ni–S, the bond length of Ni–S slightly decreases from 2.24 Å for $NiCo_2S_4$ to 2.22 Å for *a*-$NiCo_2(S_{0.84}Se_{0.16})_4$. The coordinative number (CN) of Ni–S is 3.9 for $NiCo_2S_4$, indicating a pure NiS_4 tetrahedron. For *a*-$NiCo_2(S_{0.84}Se_{0.16})_4$, the combined CN for Ni–S and Ni–Se approximates to 3.9 as well, suggesting similarly coordinatively saturated Ni(S, Se)$_4$ tetrahedra. By comparison, Se doping exhibit more obvious influence on the electronic structure of Co component. The Co K-edge XANES spectra of $NiCo_2S_4$ and *a*-$NiCo_2(S_{0.84}Se_{0.16})_4$, with standard Co foil, CoO and CoS_2 references as the controls, are shown in Fig. 4(e). The near-edge adsorption energy of Co in *a*-$NiCo_2(S_{0.84}Se_{0.16})_4$ shifts toward a lower binding energy compared with the pristine $NiCo_2S_4$, implying an increased electron density of the Co after Se doping. The Co K-edge FT-EXAFS spectra of *a*-$NiCo_2(S_{0.84}Se_{0.16})_4$ exhibit a distinct profile compared with $NiCo_2S_4$, highlighting a different Co bonding environment induced by Se doping (Fig. 4(f)). The optimal fitting results of the Co FT-EXAFS spectra are given in Figs. 4(g) and 4(h) and Table S3 in the ESM. For $NiCo_2S_4$, the most pronounced peak at 2.25 Å corresponds to the nearest Co–S bond in the first coordination shell. For *a*-$NiCo_2(S_{0.84}Se_{0.16})_4$, the first coordination shell of *R* space splits into two peaks: one at 2.21 Å assigned to the Co–S bond and the another at 2.39 Å corresponding to longer Co–Se bond. Notably, Se doping leads to a decreased radial distance of 0.04 Å for *a*-$NiCo_2(S_{0.84}Se_{0.16})_4$, suggesting a severe structural distortion after the introduction of Se. Furthermore, the CN of Co–S in $NiCo_2S_4$ and the combined CN of Co–S and Co–Se in *a*-$NiCo_2(S_{0.84}Se_{0.16})_4$ are approximately 6, suggesting a coordinative saturated octahedral structure. This finding suggests that Se doping fully substitutes S atoms without introducing additional S vacancies. The XAS analysis offers solid evidence that Se doping alters both the electronic and crystal structures of $NiCo_2S_4$, leading to the optimized surface configuration that enhances its intrinsic activity. Importantly, Se doping has a more significant impact on the electronic structure of Co compared to Ni (Fig. 4(i)). This is likely the key reason for the enhanced HER and OER activities, because Co atoms play a more prominent role in the rate-determining steps (RDSs) of these reactions, as demonstrated by theoretical calculations below.

3.2 HER and OER properties

The HER performance of *a*-$NiCo_2(S_{1-x}Se_x)_4$ was evaluated using a

three-electrode setup in 1 M KOH. The control sample of completely selenized $NiCo_2Se_4$ with similar morphology (Fig. S7 in the ESM) was also synthesized for comparison. Polarization curves (Fig. 5(a)) reveal that *a*-$NiCo_2(S_{0.84}Se_{0.16})_4$ catalyst requires only a minimal overpotential of 46 mV to achieve a current density of 10 mA·cm^{-2}, significantly lower than those of $NiCo_2S_4$ (117 mV), $NiCo_2Se_4$ (95 mV), and $NiCo_2(CO_3)_{1.5}(OH)_3$ (194 mV) and even better than that of the benchmarked Pt/C at high current densities (≥ 53 mA·cm^{-2}). Tafel slopes (Fig. 5(b)) indicate *a*-$NiCo_2(S_{0.84}Se_{0.16})_4$ has a low Tafel value of 45 mV·dec^{-1}, suggesting a Volmer–Heyrovsky mechanism with the Heyrovsky step as rate-determining step [45]. EIS measurements show significantly lower charge transfer resistance (R_{ct}) values for *a*-$NiCo_2(S_{0.84}Se_{0.16})_4$ compared with other catalysts (Fig. 5(c)), denoting faster charge transfer and more efficient kinetics for HER. Notably, the HER performance of *a*-$NiCo_2(S_{0.84}Se_{0.16})_4$ surpasses that of most previously reported non-precious HER catalysts and is even comparable to noble-metal catalysts in alkaline electrolyte (Table S4 in the ESM). Electrochemical surface area (ECSA) of *a*-$NiCo_2(S_{0.84}Se_{0.16})_4$ (26.56 mF·cm^{-2}) was determined to be 1.34 times higher than that of $NiCo_2S_4$ (Figs. S8(a)–S8(c) in the ESM), likely due to the formation of amorphous and porous structure. The current density normalized by ECSA (j_{ECSA}) of *a*-$NiCo_2(S_{0.84}Se_{0.16})_4$ is 14.1 times larger than $NiCo_2S_4$ at an overpotential of −100 mV (Fig. S8(d) in the ESM), confirming an enhancement in its intrinsic catalytic activity after Se doping. Long-term stability tests show that *a*-$NiCo_2(S_{0.84}Se_{0.16})_4$ can maintain over 95% of its initial potential after 200 h at a constant current of 100 mA·cm^{-2} (Fig. 5(g)) and meanwhile the polarization curves after 10,000 cycles show negligible degradation (Fig. S9(a) in the ESM), both confirming its good durability. Moreover, SEM, TEM and HRTEM (Fig. S10 in the ESM) along with XPS (Fig. S11 in the ESM) characterizations further disclose that *a*-$NiCo_2(S_{0.84}Se_{0.16})_4$ almost retains its original morphology, phase structure and composition after prolonged HER testing, reconfirming it excellent durability in alkaline electrolysis. To study the influence of Se/S ratio on the HER performance, *a*-$NiCo_2(S_{0.92}Se_{0.08})_4$ and $NiCo_2(S_{0.72}Se_{0.28})_4$ were also fabricated for comparation (Fig. S9(b) in the ESM). The results indicate that the HER performance initially increases and then decreases as the Se/S ratios increase.

The OER activities of the catalysts were tested in 1 M KOH electrolyte. The CV curves (Fig. 5(d)) show that *a*-$NiCo_2(S_{0.84}Se_{0.16})_4$ exhibit overpotentials of 177 mV at 10 mA·cm^{-2} and 215 mV at 100 mA·cm^{-2}, significantly lower than those acquired on $NiCo_2S_4$ (221 mV at 10 mA·cm^{-2} and 277 mV at 100 mA·cm^{-2}), $NiCo_2Se_4$ (200 mV at 10 mA·cm^{-2} and 250 mV at 100 mA·cm^{-2}), $NiCo_2(CO_3)_{1.5}(OH)_3$ (333 mV at 10 mA·cm^{-2} and 434 mV at 100 mA·cm^{-2}) and RuO_2 (196 mV at 10 mA·cm^{-2} and 292 mV at

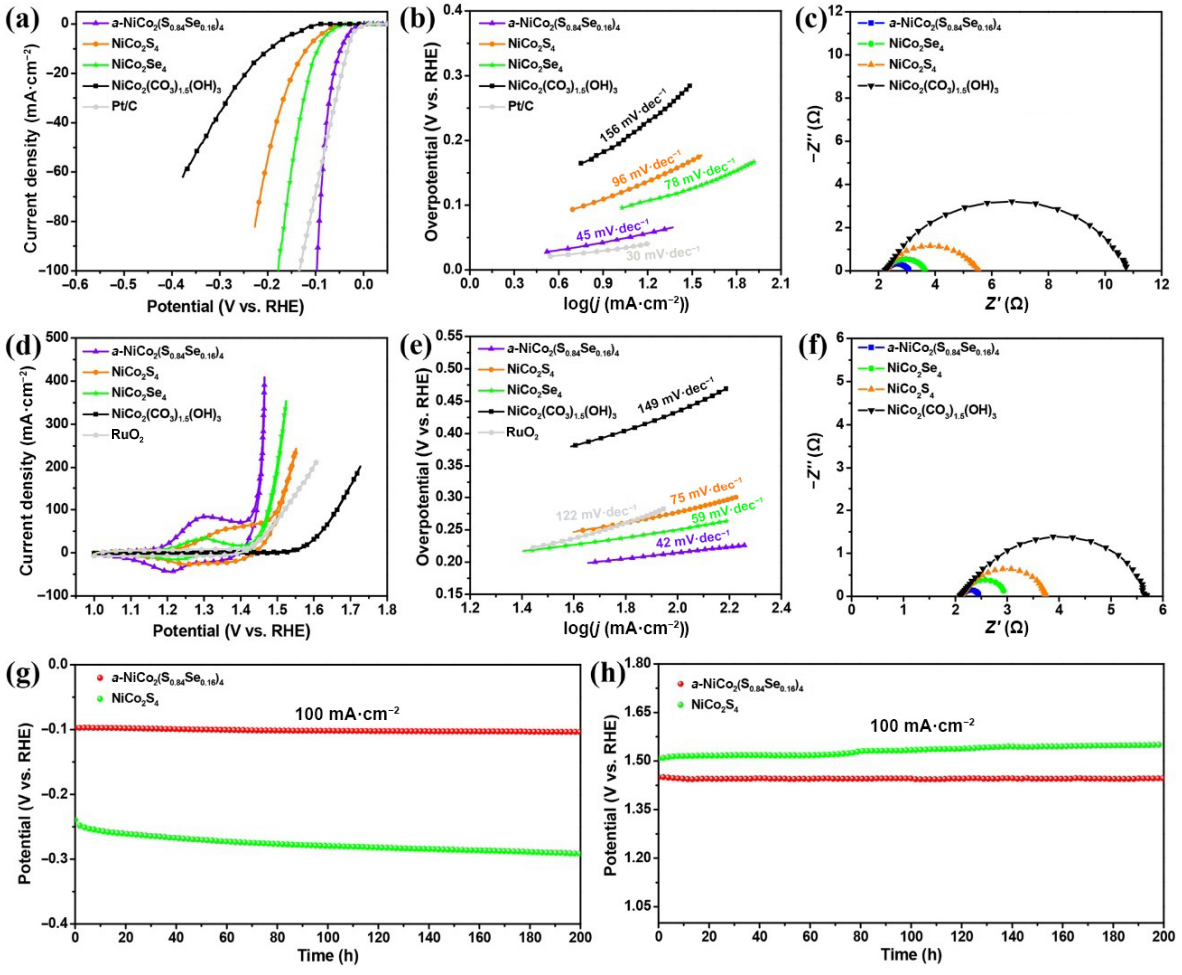

Figure 5 Electrocatalytic properties of the electrodes (*a*-$NiCo_2(S_{0.84}Se_{0.16})_4$, $NiCo_2S_4$, $NiCo_2Se_4$, $NiCo_2(CO_3)_{1.5}(OH)_3$) in alkaline electrolyte. (a) Polarization curves, (b) Tafel plots and (c) Nyquist plots of different electrodes for the HER. (d) Polarization curves, (e) Tafel plots and (f) Nyquist plots of different electrodes for the OER. (g) and (h) Long-term stability tests of the *a*-$NiCo_2(S_{0.84}Se_{0.16})_4$ and $NiCo_2S_4$ electrodes for HER and OER at a constant current density of 100 mA·cm^{-2}.

100 mA·cm^{-2}). Note that the oxidation peak of a-$NiCo_2(S_{0.84}Se_{0.16})_4$ shifts to the lower potential and meanwhile with the increase of peak area, implying that the oxidation of Ni^{2+}/Co^{2+} to Ni^{3+}/Co^{3+} is promoted by Se doping. The Ni^{3+}/Co^{3+} cathodic wave can be used to estimate the active site number, because the active materials become more electronically conductive when the Ni^{2+}/Co^{2+} species are oxidized to the Ni^{3+}/Co^{3+} species [46]. The redox wave area of a-$NiCo_2(S_{0.84}Se_{0.16})_4$ is significantly larger than that of the $NiCo_2S_4$, suggesting an increase in accessible active Ni/Co species on the former. In concert with CV result, the ECSA of a-$NiCo_2(S_{0.84}Se_{0.16})_4$ is 145% higher than that of the $NiCo_2S_4$ (Figs. S12(a)–S12(c) in the ESM). The j_{ECSA} of a-$NiCo_2(S_{0.84}Se_{0.16})_4$ is nine times that of $NiCo_2S_4$ at an overpotential of 230 mV, indicating a substantial improvement in the intrinsic activity due to Se doping (Fig. S12(d) in the ESM). Tafel slopes further validates superior OER kinetics for a-$NiCo_2(S_{0.84}Se_{0.16})_4$ (42 mV·dec^{-1}) compared to $NiCo_2S_4$ (59 mV·dec^{-1}), $NiCo_2Se_4$ (75 mV·dec^{-1}), $NiCo_2(CO_3)_{1.5}(OH)_3$ (149 mV·dec^{-1}) and RuO_2 (122 mV·dec^{-1}) (Fig. 5(e)). EIS results (Fig. 5(f)) reveal that a-$NiCo_2(S_{0.84}Se_{0.16})_4$ has the lowest R_{ct} values, suggesting it being of the best conductivity and the fastest charge transfer kinetics. The OER performance of a-$NiCo_2(S_{0.84}Se_{0.16})_4$ is very competitive, outperforming many recently reported non-noble metal-based catalysts and even matching with some noble metal-based catalysts (Table S5 in the ESM). Long-term stability tests, including CP curves at 100 mA·cm^{-2} over 200 h and 10,000 continuous CV cycles, demonstrated minimal potential variation and almost no loss of anodic current, confirming the good durability of a-$NiCo_2(S_{0.84}Se_{0.16})_4$ for OER (Fig. 5(h) and Fig. S13(a) in the ESM). Its structural robustness after CV activation was further corroborated by the XRD, TEM, HRTEM and elemental mapping analyses (Fig. S14 in the ESM), which reveal no significant changes in morphology, phase structure and elemental composition after 200 h of OER testing. To examine the impact of varying Se/S ratios on OER performance, CV curves for the samples with different Se/S ratios were analyzed (Fig. S13(b) in the ESM), revealing that a Se/S ratio of 0.197 yields the highest OER activity, again underscoring the effectiveness of Se doping in tuning the catalytic performance.

3.3 Overall water splitting

Utilizing a-$NiCo_2(S_{0.84}Se_{0.16})_4$ and $NiCo_2S_4$ as bifunctional electrocatalysts, respectively, an electrolyzer with a symmetric two-electrode setup was constructed for overall water splitting, where each material served as both anode and cathode (configured as a-$NiCo_2(S_{0.84}Se_{0.16})_4||a$-$NiCo_2(S_{0.84}Se_{0.16})_4$ and $NiCo_2S_4||NiCo_2S_4$, respectively). As shown in Fig. 6(a), a-$NiCo_2(S_{0.84}Se_{0.16})_4$ only requires a cell voltage of 1.475 V to achieve a current density of 10 mA·cm^{-2}, while this value is 1.609 V for $NiCo_2S_4$. Long-term stability testing revealed that the a-$NiCo_2(S_{0.84}Se_{0.16})_4$ based electrolyzer could maintain a near-constant voltage of 1.578 V over 200 h at 100 mA·cm^{-2} (Fig. 6(b)). As confirmed by gas chromatography, the Faradic efficiencies (FEs) for OER and HER, reached 100% with an O_2 to H_2 ratio nearly 1:2 (Fig. 6(c)). Notably, the performance of a-$NiCo_2(S_{0.84}Se_{0.16})_4||a$-$NiCo_2(S_{0.84}Se_{0.16})_4$ electrolyzer outperforms most of the high-performing catalysts designed previously for alkaline media (Table S6 in the ESM). Impressively, the system could be powered by a 1.5 V AA battery, producing visible electrolysis bubbles (Fig. 6(d)). When powered by a commercial Si solar cell with the output voltage of 1.638 V under sunlight, the system was capable of rapid and continuous generation of a large number of bubbles at both electrodes (Figs. 6(e) and 6(f) and Video S1 in the ESM), showcasing its potential for practical energy conversion applications.

3.4 HER and OER enhancement mechanism

Before each HER polarization curve measurement, the cathode material underwent 20 CV cycles to stabilize the polarization curve. Post-cycling characterization of a-$NiCo_2(S_{0.84}Se_{0.16})_4$ (Fig. S15 in the ESM) showed that the morphology, structure and composition remained unchanged compared to the initial catalyst, indicating no

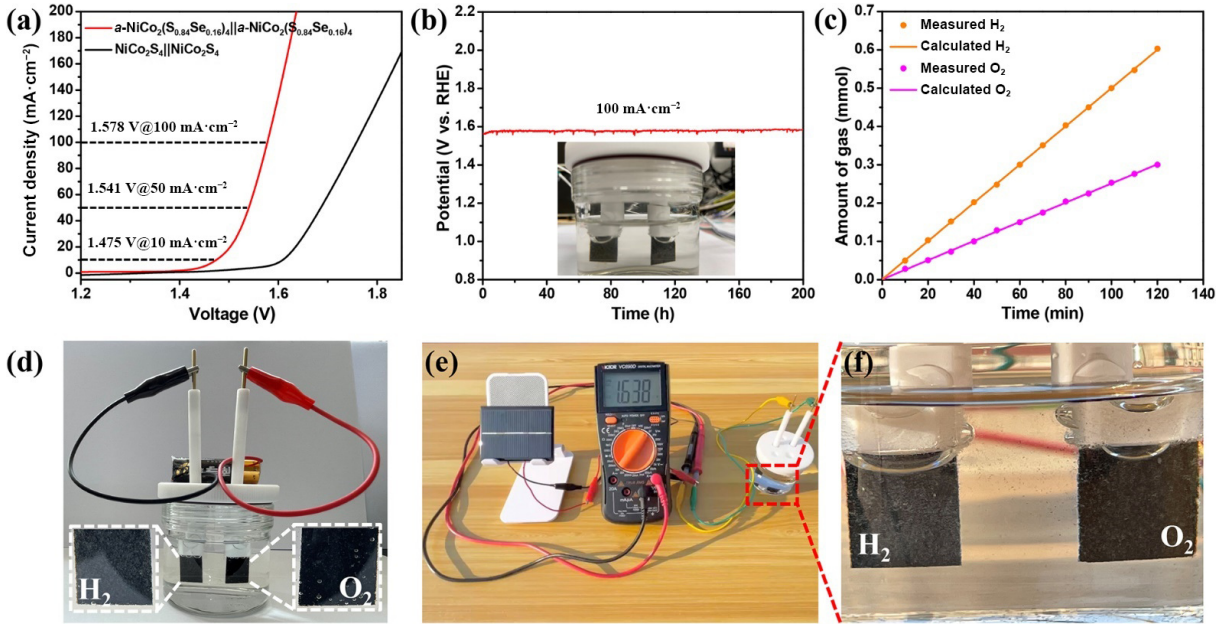

Figure 6 (a) LSV curves of the electrocatalysts for overall water splitting in a two-electrode alkaline electrolyzer. (b) Chronopotentiometric curve of water electrolysis at a constant current density of 100 mA·cm^{-2}. (c) Time evolution of the amount of produced gas with respect to the theoretically calculated values for the overall water splitting. (d) Photo of the electrolyzer powered by a single AA battery (1.5 V). (e) Voltage demonstration of solar cells under sunlight (ca. 1.638 V). (f) Demonstration of the evolution of H_2 and O_2 gases on a-$NiCo_2(S_{0.84}Se_{0.16})_4$/CFP$||a$-$NiCo_2(S_{0.84}Se_{0.16})_4$/CFP.

morphological or phase transitions. Similar stability was observed for $NiCo_2S_4$ after 20 CV cycles (Fig. S16 in the ESM). Consequently, the initial crystal structure and planes were used as the model for the DFT calculations to represent the catalyst's active sites during the HER process.

Since experimental results identified the (311) surface of $NiCo_2S_4$ as the dominant exposed crystal surface, (311) surface models of $NiCo_2S_4$ and *a*-$NiCo_2(S_{1-x}Se_x)_4$ were particularly constructed for DFT calculations (Fig. S17 in the ESM). The optimized atomic configurations of the water dissociation step show that both Co and Ni sites involve H_2O dissociation process, where H_2O molecules are first adsorbed at the Co site and then activated and electrochemically dissociated thereon. The generated OH^- species are adsorbed on Co–Co bridge sites while the intermediate H_{ads} transfer to adjacent Ni sites (Fig. 7(a) and Fig. S18 in the ESM). So the detail HER mechanism for *a*-$NiCo_2(S_{1-x}Se_x)_4$ catalysts is speculated as the followings based on the DFT calculations (Fig. 7(b)): this process includes H_2O adsorption, reduction to generate H and OH^-, adsorption and desorption of OH^- and formation of H intermediates for hydrogen evolution in sequence. The kinetic energy barrier of the initial Volmer step (ΔG (H_2O) was examined (Fig. 7(c)), revealing that $NiCo_2S_4$ has a rather high water dissociation energy barrier (ΔG (H_2O) = 1.115 eV) so as to cause a slow Volmer step. In contrast, *a*-$NiCo_2(S_{1-x}Se_x)_4$ can significantly reduce ΔG (H_2O) to 0.267 eV, accelerating the otherwise sluggish Volmer step. Furthermore, *a*-$NiCo_2(S_{1-x}Se_x)_4$ exhibits a lower ΔG_{H^*} of 0.327 eV compared to 0.434 eV for $NiCo_2S_4$, confirming its superior hydrogen adsorption capability (Fig. 7(d)). Since the ΔG (H_2O) is lower than ΔG_{H^*}, the Heyrovsky step rather than the Volmer step is identified as the rate-determining step of HER on *a*-$NiCo_2(S_{1-x}Se_x)_4$, consistent with electrochemical testing results. Additionally, the impact of Se doping on the electronic structure of $NiCo_2S_4$ was verified through DOS analyses (Figs. S19 and S20 in the ESM and Fig. 7(e)). The total DOS (TDOS) indicates that both $NiCo_2S_4$ and *a*-$NiCo_2(S_{1-x}Se_x)_4$ exhibit intrinsic metallic properties due to sequential DOS around the Fermi level. *a*-$NiCo_2(S_{1-x}Se_x)_4$ displays a higher DOS at the Fermi level than $NiCo_2S_4$, suggesting a higher electrical conductivity due to a greater carrier concentration [47]. Se doping also shifts the d-band center of Co and Ni orbitals from −0.6801 to −0.6440 and from −0.7926 to −0.7731 eV, respectively (Fig. S20 in the ESM and Fig. 7(e)). The shallower d-band center of Co and Ni typically leads to stronger H_2O adsorption in favor of H_2O dissociation and stronger H adsorption, respectively, which accounts for the observed change in ΔG (H_2O) and ΔG_{H^*}. Importantly, the change of d-band center and ΔG (H_2O) for Co sites is greater than that of ΔG_{H^*} for the Ni sites after Se doping. This indicates that the Se doping has a more pronounced impact on electronic structure of Co more than Ni, consistent with XAS results.

Previous studies have shown that transition metal chalcogenide-based anodes generally transform into metal oxyhydroxides during OER testing [48–50]. In our study, *a*-$NiCo_2(S_{0.84}Se_{0.16})_4$ undergone a complete reconstruction into Se, S co-doped $Ni_{0.33}Co_{0.67}OOH$ (S, Se-$Ni_{0.67}Co_{0.33}OOH$) ultrathin nanosheets, preserving the array structure after CV activation prior to OER testing. XRD, SEM and TEM analyses confirm the transformation of *a*-$NiCo_2(S_{0.84}Se_{0.16})_4$ into hierarchical architectures, which compose predominantly of poor crystalline Ni-CoOOH nanosheets (Figs. 8(a)–8(e) and Fig. S21 in the ESM). EDX mappings (Figs. 8(f) and 8(g)) show a uniform distribution of Ni, Co, O, S and Se. The EDX spectrum (Fig. 8(h)) indicate a composition primarily of Ni (11.4 at.%), Co (21.7 at.%) and O (61.2 at.%) with minor S (3.9 at.%) and Se (1.8

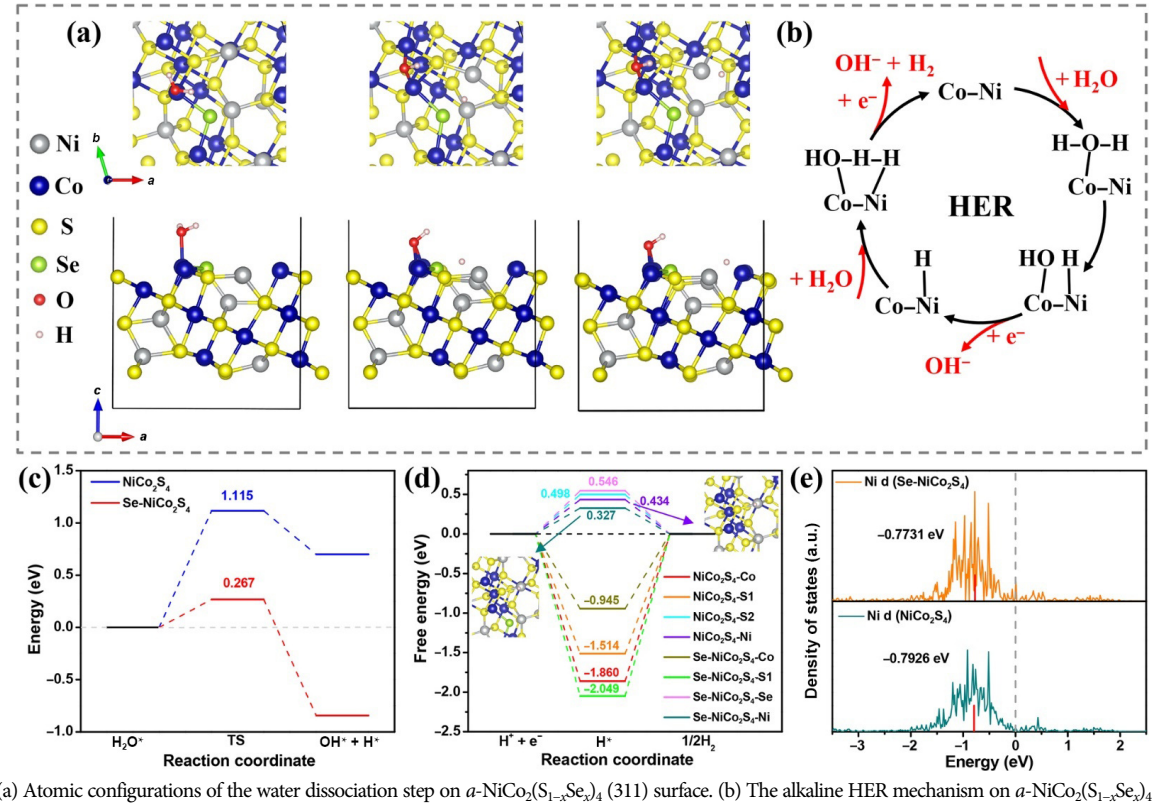

Figure 7 (a) Atomic configurations of the water dissociation step on *a*-$NiCo_2(S_{1-x}Se_x)_4$ (311) surface. (b) The alkaline HER mechanism on *a*-$NiCo_2(S_{1-x}Se_x)_4$ catalysts. (c) Calculated reaction energy diagram of water dissociation into H* and OH* on the $NiCo_2Se_4$ (311) and *a*-$NiCo_2(S_{1-x}Se_x)_4$ (311) facets. (d) Free energy diagram of HER on different sites of the $NiCo_2Se_4$ (311) and *a*-$NiCo_2(S_{1-x}Se_x)_4$ (311) facets; and (e) the PDOS of the Ni d-orbital of the $NiCo_2Se_4$ (311) and *a*-$NiCo_2(S_{1-x}Se_x)_4$ (311) facets.

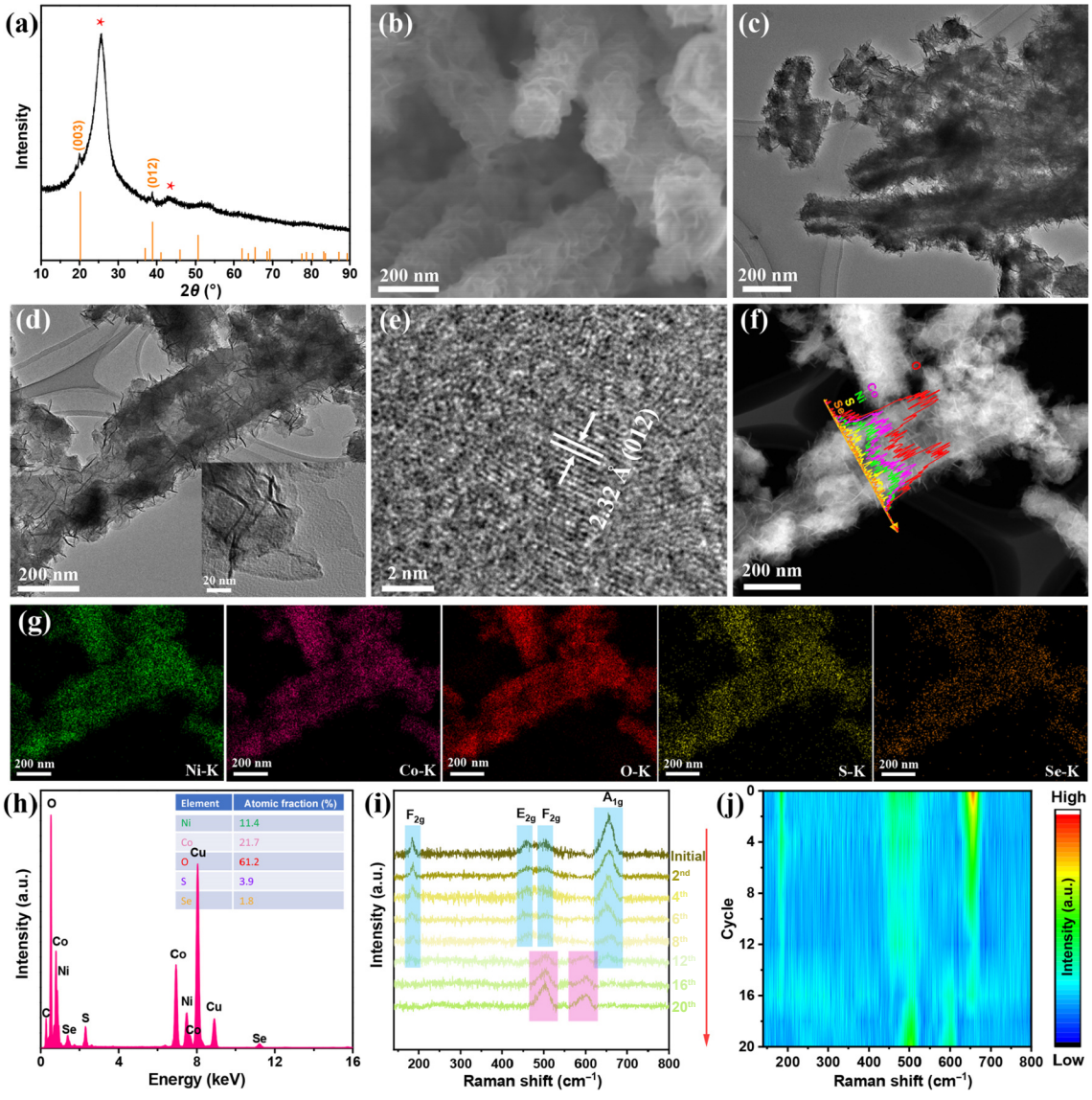

Figure 8 (a) The XRD pattern, (b) SEM image, (c) and (d) TEM images (inset: high-magnification TEM), (e) HRTEM image, (f) HAADF-STEM, (g) corresponding elemental mapping images and (h) EDX spectra of *a*-$NiCo_2(S_{0.84}Se_{0.16})_4$ after CV activation. (i) *In situ* Raman spectra and (j) corresponding contour plots of *a*-$NiCo_2(S_{1-x}Se_x)_4$ at different CV cycle number from 0 to 20th.

at.%), suggesting a significant oxidation loss of initial S and Se. XPS analyses (Fig. S22 in the ESM) reveal the shifts of the Ni 2p and Co 2p peaks towards higher binding energies after structural reconstruction, indicating the existence of predominant Ni^{3+} and Co^{3+} states [51, 52]. Closer inspection of the weak S 2p and Se 3d peaks confirm the presence of metal–S and metal–Se bonds after structural reconstruction, implying that the residual S and Se doped into the catalyst. To gain a deeper understanding of the reconstruction process, we conducted *in situ* Raman investigation on the evolution of *a*-$NiCo_2(S_{1-x}Se_x)_4$ under OER conditions (Fig. S23 in the ESM). The initial *a*-$NiCo_2(S_{1-x}Se_x)_4$ samples display four characteristic Raman peaks corresponding to the F_{2g} (185 cm^{-1}), E_{2g} (460 cm^{-1}), F_{2g} (505 cm^{-1}) and A_{1g} (658 cm^{-1}) phonon modes of $NiCo_2S_4$ (Fig. 8(i)) [53]. These characteristic Raman peaks gradually disappear during OER, indicating the breakdown of M–S/Se bonds and leaching of S/Se. While the appearance of new peaks at 503 and 601 cm^{-1} indicate the formation of CoOOH species (Figs. 8(i) and 8(j)) [54]. Apparently, above Raman results highlight the dynamic reconstruction and active species evolution in these catalyst systems. Similarly, $NiCo_2S_4$ also transforms into S doped Ni-CoOOH nanosheets (S-$Ni_{0.33}Co_{0.67}OOH$) after CV activation, as confirmed by XRD, SEM, TEM and EDX analyses (Fig. S24 in the ESM). However, in comparison, the S-$Ni_{0.33}Co_{0.67}OOH$ derived from $NiCo_2S_4$ retains a relatively intact crystal structure with smaller layers, while the S, Se-$Ni_{0.67}Co_{0.33}OOH$ from *a*-$NiCo_2(S_{0.84}Se_{0.16})_4$ is nearly fully amorphized with larger layer size. This interesting phenomenon implies that Se doping facilitates not only the complete structural reconstruction but also the amorphous structure formation for Ni-CoOOH, thereby enhancing its catalytic activity.

To explore the origin of the OER activity of the *in situ* formed S-$Ni_{0.67}Co_{0.33}OOH$ and S, Se-$Ni_{0.67}Co_{0.33}OOH$, the DFT calculations were conducted. We modeled the surface slab of S-$Ni_{0.67}Co_{0.33}OOH$ (001) surface and S, Se-$Ni_{0.67}Co_{0.33}OOH$ (001) (Fig. S25 in the ESM). The optimized atomic configurations of oxygen intermediates (*OH, *O and *OOH) adsorbed on the both surfaces

are presented in Fig. 9(a) and Fig. S26 in the ESM. The results reveal that the Co–Co bridge sites are the optimal absorption sites for the intermediates (*OH, *O and *OOH). The schematic of typical four-reaction OER mechanism on Se, S-$Ni_{0.67}Co_{0.33}OOH$ can thus be presented as Fig. 9(b). The process includes: (i) adsorption of an OH^- ion at the Co–Co bridge sites (*OH); (ii) reaction of *OH with another OH^- ion to form an O group (*O); (iii) reaction of *O with another OH^- ion to form an OOH group (*OOH); and (iv) formation and release of O_2. Each step involves the absorption of an OH^- anion and the release of an electron on Co sites. More importantly, the Gibbs free energy for each step was calculated to identify the RDS and estimate the theoretical overpotential (Fig. 9(c)). Evidently, the RDS for Se, S-$Ni_{0.67}Co_{0.33}OOH$ involves the O–O coupling process, exhibiting a rather low theoretical overpotential of 1.58 V. In comparison, the RDS for S-$Ni_{0.67}Co_{0.33}OOH$ is the desorption of O_2, with a much higher theoretical overpotential of 2.88 V.

The d-band center is a good active indicator for the adsorbate–metal interaction [55, 56]. For S-$Ni_{0.67}Co_{0.33}OOH$ and Se, S-$Ni_{0.67}Co_{0.33}OOH$, the d-band center values were determined to be −0.721 and −0.769 eV, respectively according to their partial DOS (PDOS) spectra (Fig. 9(d)). Typically, the electronic interaction between the valence states of adsorbed molecules and the d states of transition metals lead to the formation of separated bonding and antibonding states, as depicted in Fig. 9(e). A decreased d-band center value results in a downward shift of the antibonding states, allowing more electrons to fill these orbitals so as to weaken the binding to the adsorbates [57]. Combined with above XAS analysis, we thus speculate that Se doping can effectively tune the d-orbitals of the active Co atoms to optimize the adsorption for OER intermediates, accounting for the superior OER activity of Se, S-$Ni_{0.67}Co_{0.33}OOH$.

4 Conclusions

In conclusion, we developed an ultrafast and mild electrochemical doping method to prepare Se doped $NiCo_2S_4$ nanoarrays with SeO_2 solution as the electrolyte. The unique adsorption behavior of Se species on $NiCo_2S_4$ enables the cathode to prioritize Se doping reaction over low barrier HER under an applied reduction potential of −0.8 V vs. Ag/AgCl. The doping mechanism involves the substitution of S atoms in $NiCo_2S_4$ with Se atoms. A systematic experimental and theoretical investigation reveals the significant influences of Se doping on the electronic structure and reconstruction behavior of $NiCo_2S_4$. Specifically, under HER conditions, the *a*-$NiCo_2(S_{0.84}Se_{0.16})_4$ demonstrates remarkable stability, with Se tuning the electronic structure to optimize intermediate adsorption and facilitate H_2O dissociation. While under OER conditions, Se doping lowers the energy barrier for reconstruction and promotes phase transformation into highly active Se, S-$Ni_{0.33}Co_{0.67}OOH$ ultrathin nanosheets. Moreover, the Se doping has a more pronounced impact on electronic structure of Co more than Ni. This is likely a crucial factor in the marked enhancement of electrocatalytic activity via Se doping, because Co atoms play a more prominent role in the rate-determining steps of these reactions. Besides, the Se doping leads to amorphous structure in both *a*-$NiCo_2(S_{0.84}Se_{0.16})_4$ and reconstructed Se, S-$Ni_{0.33}Co_{0.67}OOH$, further enhancing the electrocatalytic performance. The optimal samples exhibit high electrocatalytic activity and outstanding durability, delivering a current density of 100 mA·cm^{-2} at overpotentials of 98 mV for HER and 215 mV for

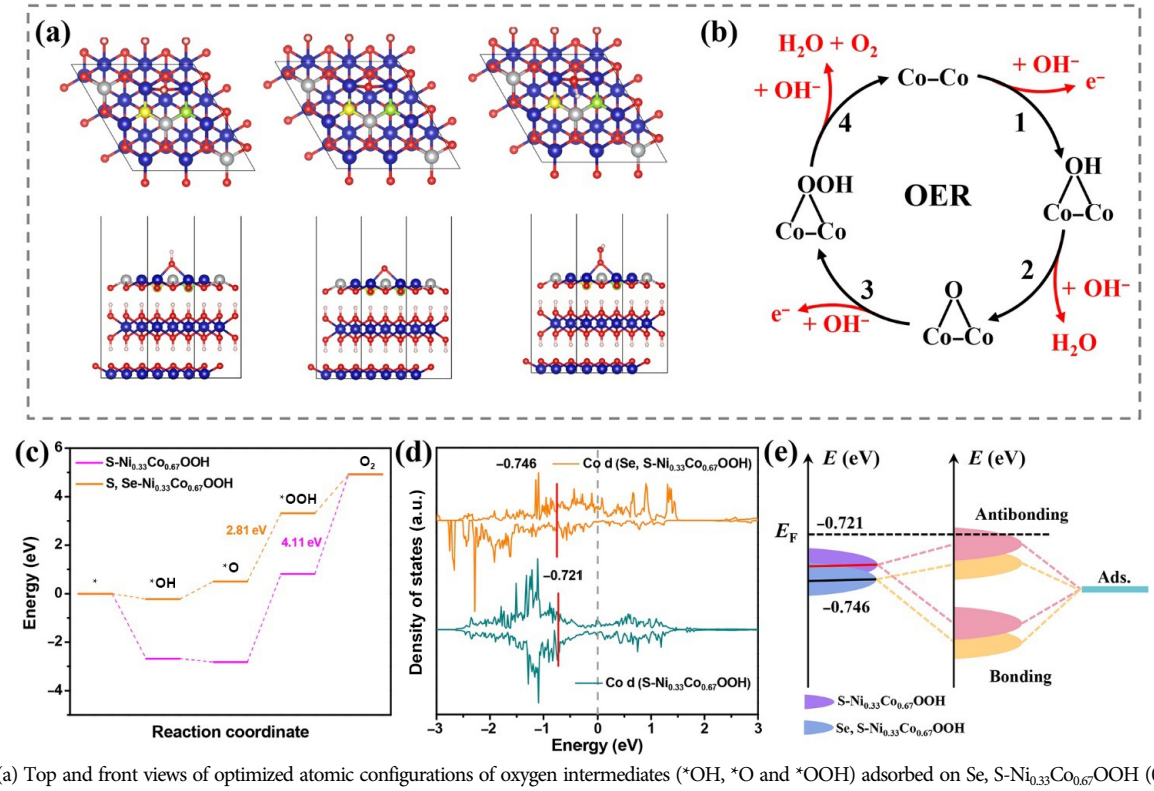

Figure 9 (a) Top and front views of optimized atomic configurations of oxygen intermediates (*OH, *O and *OOH) adsorbed on Se, S-$Ni_{0.33}Co_{0.67}OOH$ (001) surface. (b) Four-step adsorbate evolution mechanism for Se, S-$Ni_{0.33}Co_{0.67}OOH$. (c) The Gibbs free energy change diagrams of the OER process on the S-$Ni_{0.33}Co_{0.67}OOH$ (magenta) and Se, S-$Ni_{0.33}Co_{0.67}OOH$ (orange) surface models (all terminated with (001) facet). (d) The PDOS of the Co d-orbital of the S-$Ni_{0.33}Co_{0.67}OOH$ (001) and Se, S-$Ni_{0.33}Co_{0.67}OOH$ (001) facets. (e) Schematic illustration of bond formation between the catalyst surface and the adsorbates (Ads.).

OER, respectively. Impressively, a water electrolyzer equipped with this bifunctional electrode requires a low cell voltage of 1.578 V to obtain 100 $mA \cdot cm^{-2}$ for overall water splitting with negligible performance degradation over 200 h. This work not only introduces a facile method for Se doping but also provides comprehensive insights into the structure–composition–activity relationship for Se-doped bimetallic sulfide.

Electronic Supplementary Material: Supplementary material (additional characterization results, electrochemical data and DFT computational results) is available in the online version of this article at https://doi.org/10.26599/NR.2025.94907165.

Data availability

All data needed to support the conclusions in the paper are presented in the manuscript and the Electronic Supplementary Material. Additional data related to this paper may be requested from the corresponding author upon request.

Acknowledgements

This work was financially supported by the National Natural Science Foundation of China (Nos. 22272008 and 21872011) and the Project of PetroChina Technology Management Department (No. 2023ZZ1202).

Declaration of competing interest

All the contributing authors report no conflict of interests in this work.

Author contribution statement

G. J. W.: Conceptualization, methodology, investigation, data curation, visualization, formal analysis, writing – original draft. Y. Z. S.: Investigation, software, formal analysis, visualization, validation. Y. D. Z.: Investigation, validation, data curation. C. D.: Investigation, validation, visualization. Y. Z. Z.: supervision, writing – review & editing. Y. C. L.: Supervision, funding acquisition, project administration, writing – review & editing. All the authors have approved the final manuscript.

Use of AI statement

None.

References

[1] You, B.; Sun, Y. J. Innovative strategies for electrocatalytic water splitting. *Acc. Chem. Res.* **2018**, *51*, 1571–1580.

[2] Sun, H. M.; Yan, Z. H.; Liu, F. M.; Xu, W. C.; Cheng, F. Y.; Chen, J. Self-supported transition-metal-based electrocatalysts for hydrogen and oxygen evolution. *Adv. Mater.* **2020**, *32*, 1806326.

[3] Chen, H. Y.; Yu, J. D.; Liu, L. J.; Gao, R. T.; Gao, Z. H.; Yang, Y.; Chen, Z. Q.; Zhan, S. B.; Liu, X. H.; Zhang, X. Y. et al. Modulating Pt-N/O bonds on co-doped WO_3 for acid electrocatalytic hydrogen evolution with over 2000 h operation. *Adv. Energy Mater.* **2024**, *14*, 2303635.

[4] Hu, C. L.; Zhang, L.; Gong, J. L. Recent progress made in the mechanism comprehension and design of electrocatalysts for alkaline water splitting. *Energy Environ. Sci.* **2019**, *12*, 2620–2645.

[5] Hou, J. G.; Wu, Y. Z.; Zhang, B.; Cao, S. Y.; Li, Z. W.; Sun, L. C. Rational design of nanoarray architectures for electrocatalytic water splitting. *Adv. Funct. Mater.* **2019**, *29*., 1808367.

[6] Chen, H. Y.; Gao, R. T.; Chen, H. J.; Yang, Y.; Wu, L. M.; Wang, L. Ruthenium and silver synergetic regulation NiFe LDH boosting long-duration industrial seawater electrolysis. *Adv. Funct. Mater.* **2024**, *34*, 2315674.

[7] Wang, L.; Gao, Z. H.; Su, K. R.; Nguyen, N. T.; Gao, R. T.; Chen, J. X.; Wang, L. Stacked high-entropy hydroxides promote charge transfer kinetics for photoelectrochemical water splitting. *Adv. Funct. Mater.* **2024**, *34*, 2403948.

[8] Sun, L.; Luo, Q. M.; Dai, Z. F.; Ma, F. Material libraries for electrocatalytic overall water splitting. *Coord. Chem. Rev.* **2021**, *444*, 214049.

[9] Kim, H. J.; Kim, H. Y.; Joo, J.; Joo, S. H.; Lim, J. S.; Lee, J.; Huang, H. W.; Shao, M. H.; Hu, J.; Kim, J. Y. et al. Recent advances in non-precious group metal-based catalysts for water electrolysis and beyond. *J. Mater. Chem. A* **2022**, *10*, 50–88.

[10] Wang, J.; Zang, N.; Xuan, C. J.; Jia, B. H.; Jin, W.; Ma, T. Y. Self-supporting electrodes for gas-involved key energy reactions. *Adv. Funct. Mater.* **2021**, *31*, 2104620.

[11] Li, M.; Feng, L. G. $NiSe_2$-$CoSe_2$ with a hybrid nanorods and nanoparticles structure for efficient oxygen evolution reaction. *Chin. J. Struct. Chem* **2022**, *41*, 2201019–2201024.

[12] An, Z. Y.; Xue, H.; Sun, J.; Guo, N. K.; Song, T. S.; Sun, J. W.; Hao, Y. R.; Wang, Q. Co-construction of sulfur vacancies and heterogeneous interface into Ni_3S_2/MoS_2 catalysts to achieve highly efficient overall water splitting. *Chin. J. Struct. Chem* **2022**, *41*, 2208037–2208043.

[13] Liu, X.; Meng, J. S.; Zhu, J. X.; Huang, M.; Wen, B.; Guo, R. T.; Mai, L. Q. Comprehensive understandings into complete reconstruction of precatalysts: Synthesis, applications, and characterizations. *Adv. Mater.* **2021**, *33*, 2007344.

[14] Li, Y. Y.; Du, X. C.; Huang, J. W.; Wu, C. Y.; Sun, Y. H.; Zou, G. F.; Yang, C. T.; Xiong, J. Recent progress on surface reconstruction of earth-abundant electrocatalysts for water oxidation. *Small* **2019**, *15*, 1901980.

[15] Xiong, B. Y.; Chen, L. S.; Shi, J. L. Anion-containing noble-metal-free bifunctional electrocatalysts for overall water splitting. *ACS Catal.* **2018**, *8*, 3688–3707.

[16] Fu, G. T.; Lee, J. M. Ternary metal sulfides for electrocatalytic energy conversion. *J. Mater. Chem. A* **2019**, *7*, 9386–9405.

[17] Kang, Z.; Guo, H. J.; Wu, J.; Sun, X.; Zhang, Z.; Liao, Q. L.; Zhang, S. C.; Si, H. N.; Wu, P. W.; Wang, L. et al. Engineering an earth-abundant element-based bifunctional electrocatalyst for highly efficient and durable overall water splitting. *Adv. Funct. Mater.* **2019**, *29*, 1807031.

[18] Xue, Y. R.; Zuo, Z. C.; Li, Y. J.; Liu, H. B.; Li, Y. L. Graphdiyne-supported $NiCo_2S_4$ nanowires: A highly active and stable 3D bifunctional electrode material. *Small* **2017**, *13*, 1700936.

[19] Lee, H. S.; Pan, J.; Gund, G. S.; Park, H. S. Vertically aligned $NiCo_2S_4$ nanosheets deposited on N-doped graphene for bifunctional and durable electrode of overall water splitting. *Adv. Mater. Interfaces* **2020**, *7*, 2000138.

[20] Li, F.; Xu, R. C.; Li, Y. M.; Liang, F.; Zhang, D. F.; Fu, W. F.; Lv, X. J. N-doped carbon coated $NiCo_2S_4$ hollow nanotube as bifunctional electrocatalyst for overall water splitting. *Carbon* **2019**, *145*, 521–528.

[21] Sivanantham, A.; Ganesan, P.; Shanmugam, S. Hierarchical $NiCo_2S_4$ nanowire arrays supported on Ni foam: An efficient and durable bifunctional electrocatalyst for oxygen and hydrogen evolution reactions. *Adv. Funct. Mater.* **2016**, *26*, 4661–4672.

[22] Zhang, A.; Liang, Y. X.; Zhang, H.; Geng, Z. G.; Zeng, J. Doping regulation in transition metal compounds for electrocatalysis. *Chem. Soc. Rev.* **2021**, *50*, 9817–9844.

[23] Sun, Y. Q.; Zhang, T.; Li, C. C.; Xu, K.; Li, Y. Compositional engineering of sulfides, phosphides, carbides, nitrides, oxides, and hydroxides for water splitting. *J. Mater. Chem. A* **2020**, *8*, 13415–13436.

[24] Wang, J.; Liao, T.; Wei, Z. Z.; Sun, J. T.; Guo, J. J.; Sun, Z. Q.

Heteroatom-doping of non-noble metal-based catalysts for electrocatalytic hydrogen evolution: An electronic structure tuning strategy. *Small Methods* **2021**, *5*, 2000988.
[25] Dyjak, S.; Jankiewicz, B. J.; Kaniecki, S.; Kiciński, W. Selenium-doped carbon materials: Synthesis and applications for sustainable technologies. *Green Chem.* **2024**, *26*, 2985–3020.
[26] Zhuo, J. Q.; Cabán-Acevedo, M.; Liang, H. F.; Samad, L.; Ding, Q.; Fu, Y. P.; Li, M. X.; Jin, S. High-performance electrocatalysis for hydrogen evolution reaction using se-doped pyrite-phase nickel diphosphide nanostructures. *ACS Catal.* **2015**, *5*, 6355–6361.
[27] Wang, K.; Zhou, C. J.; Xi, D.; Shi, Z. Q.; He, C.; Xia, H. Y.; Liu, G. W.; Qiao, G. J. Component-controllable synthesis of $Co(S_xSe_{1-x})_2$ nanowires supported by carbon fiber paper as high-performance electrode for hydrogen evolution reaction. *Nano Energy* **2015**, *18*, 1–11.
[28] Niu, S.; Jiang, W. J.; Wei, Z. X.; Tang, T.; Ma, J. M.; Hu, J. S.; Wan, L. J. Se-doping activates FeOOH for cost-effective and efficient electrochemical water oxidation. *J. Am. Chem. Soc.* **2019**, *141*, 7005–7013.
[29] Wang, Q. T.; Huang, Y. N.; Huang, L. Q.; Wu, Y. X.; Ren, S. F. Se doping regulates the activity of $NiTe_2$ for electrocatalytic hydrogen evolution reaction. *J. Phys. Chem. C* **2020**, *124*, 26793–26800.
[30] Zhang, B. L.; Qian, X. Y.; Xu, H.; Jiang, L.; Xia, J. W.; Chen, H. Q.; He, G. Y. Se-doping-induced sulfur vacancy engineering of $CuCo_2S_4$ nanosheets for enhanced electrocatalytic overall water splitting. *Nanoscale* **2023**, *15*, 16199–16208.
[31] Li, B. S.; Li, J. P.; Liu, X. W.; Guo, J. X.; Sun, Y. F.; Zhang, X. Se-doped CoP nanoneedle arrays grown on carbon cloth for an efficient hydrogen evolution reaction. *Energy Fuels* **2022**, *36*, 13212–13217.
[32] Du, X. Q.; Ding, Y. Y.; Zhang, X. S. Selectively Se-doped Co_3O_4@CeO_2 nanoparticle-dotted nanoneedle arrays for high-efficiency overall water splitting. *Appl. Surf. Sci.* **2021**, *562*, 150227.
[33] Kresse, G.; Furthmüller, J. Efficiency of *ab-initio* total energy calculations for metals and semiconductors using a plane-wave basis set. *Comput. Mater. Sci.* **1996**, *6*, 15–50.
[34] Kresse, G.; Furthmüller, J. Efficient iterative schemes for *ab initio* total-energy calculations using a plane-wave basis set. *Phys. Rev. B* **1996**, *54*, 11169–11186.
[35] Kresse, G.; Joubert, D. From ultrasoft pseudopotentials to the projector augmented-wave method. *Phys. Rev. B* **1999**, *59*, 1758–1775.
[36] Perdew, J. P.; Chevary, J. A.; Vosko, S. H.; Jackson, K. A.; Pederson, M. R.; Singh, D. J.; Fiolhais, C. Atoms, molecules, solids, and surfaces: Applications of the generalized gradient approximation for exchange and correlation. *Phys. Rev. B* **1992**, *46*, 6671–6687.
[37] Perdew, J. P.; Burke, K.; Ernzerhof, M. Generalized gradient approximation made simple. *Phys. Rev. Lett.* **1996**, *77*, 3865–3868.
[38] Nørskov, J. K.; Bligaard, T.; Logadottir, A.; Kitchin, J. R.; Chen, J. G.; Stimming, U. Trends in the exchange current for hydrogen evolution. *J. Electrochem. Soc.* **2005**, *152*, J23–J26.
[39] Nørskov, J. K.; Rossmeisl, J.; Logadottir, A.; Lindqvist, L.; Kitchin, J. R.; Bligaard, T.; Jónsson, H. Origin of the overpotential for oxygen reduction at a fuel-cell cathode. *J. Phys. Chem. B* **2004**, *108*, 17886–17892.
[40] Naveau, A.; Monteil-Rivera, F.; Guillon, E.; Dumonceau, J. Interactions of aqueous selenium(−II) and (IV) with metallic sulfide surfaces. *Environ. Sci. Technol.* **2007**, *41*, 5376–5382.
[41] Sun, Y. Y.; Zhang, X. Y.; Tang, J. F.; Li, X. X.; Fu, H. Q.; Xu, H. G.; Mao, F. X.; Liu, P. F.; Yang, H. G. Amorphous oxysulfide reconstructed from spinel $NiCo_2S_4$ for efficient water oxidation. *Small* **2023**, *19*, 2207965.
[42] Liu, J.; Meng, X.; Xie, J. H.; Liu, B.; Tang, B.; Wang, R. Y.; Wang, C.; Gu, P.; Song, Y. D.; Huo, S. C. et al. Dual active sites engineering on sea urchin-Like CoNiS hollow nanosphere for stabilizing oxygen electrocatalysis via a template-free vulcanization strategy. *Adv. Funct. Mater.* **2023**, *33*, 2300579.
[43] Yu, J. Q.; Cai, D. P.; Si, J. H.; Zhan, H. B.; Wang, Q. T. MOF-derived $NiCo_2S_4$ and carbon hybrid hollow spheres compactly concatenated by electrospun carbon nanofibers as self-standing electrodes for aqueous alkaline Zn batteries. *J. Mater. Chem. A* **2022**, *10*, 4100–4109.
[44] Li, Y.; Gao, Y. A.; Yang, S.; Wu, C. Q.; Tan, Y. W. Anion-modulated nickel-based nanoheterostructures as high performance electrocatalysts for hydrogen evolution reaction. *J. Mater. Chem. A* **2020**, *8*, 12013–12027.
[45] Wu, J.; Chen, T.; Zhu, C. Y.; Du, J. J.; Huang, L. S.; Yan, J.; Cai, D. M.; Guan, C.; Pan, C. X. Rational construction of a WS_2/CoS_2 heterostructure electrocatalyst for efficient hydrogen evolution at all pH values. *ACS Sustain. Chem. Eng.* **2020**, *8*, 4474–4480.
[46] Batchellor, A. S.; Boettcher, S. W. Pulse-electrodeposited Ni–Fe (oxy)hydroxide oxygen evolution electrocatalysts with high geometric and intrinsic activities at large mass loadings. *ACS Catal.* **2015**, *5*, 6680–6689.
[47] Liu, C. C.; Jia, D. B.; Hao, Q. Y.; Zheng, X. R.; Li, Y.; Tang, C. C.; Liu, H.; Zhang, J.; Zheng, X. L. P-doped iron-nickel sulfide nanosheet arrays for highly efficient overall water splitting. *ACS Appl. Mater. Interfaces* **2019**, *11*, 27667–27676.
[48] Tang, C.; Cheng, N. Y.; Pu, Z. H.; Xing, W.; Sun, X. P. NiSe nanowire film supported on nickel foam: An efficient and stable 3D bifunctional electrode for full water splitting. *Angew. Chem., Int. Ed.* **2015**, *54*, 9351–9355.
[49] Yang, L.; Qin, H. Y.; Dong, Z. H.; Wang, T. Z.; Wang, G. C.; Jiao, L. F. Metallic S-CoTe with surface reconstruction activated by electrochemical oxidation for oxygen evolution catalysis. *Small* **2021**, *17*, 2102027.
[50] Zhou, M.; Weng, Q. H.; Zhang, X. Y.; Wang, X.; Xue, Y. M.; Zeng, X. H.; Bando, Y.; Golberg, D. *In situ* electrochemical formation of core–shell nickel-iron disulfide and oxyhydroxide heterostructured catalysts for a stable oxygen evolution reaction and the associated mechanisms. *J. Mater. Chem. A* **2017**, *5*, 4335–4342.
[51] Zhao, W. P.; Peng, C. L.; Kuang, Z. Y.; Zhang, Q. M.; Xue, Y.; Li, Z. X.; Zhou, X. X.; Chen, H. R. Na^+-induced *in situ* reconstitution of metal phosphate enabling efficient electrochemical water oxidation in neutral and alkaline media. *Chem. Eng. J.* **2020**, *398*, 125537.
[52] Fan, K.; Zou, H. Y.; Lu, Y.; Chen, H.; Li, F. S.; Liu, J. X.; Sun, L. C.; Tong, L. P.; Toney, M. F.; Sui, M. L. et al. Direct observation of structural evolution of metal chalcogenide in electrocatalytic water oxidation. *ACS Nano* **2018**, *12*, 12369–12379.
[53] Fan, S. S.; Liu, H. P.; Bi, S. F.; Gao, C.; Meng, X. H.; Wang, Y. N. Insight on the conversion reaction mechanism of $NiCo_2S_4$@CNTs as anode materials for lithium ion batteries and sodium ion batteries. *Electrochim. Acta* **2021**, *388*, 138618.
[54] Wang, M.; Dong, C. L.; Huang, Y. C.; Shen, S. H. *Operando* spectral and electrochemical investigation into the heterophase stimulated active species transformation in transition-metal sulfides for efficient electrocatalytic oxygen evolution. *ACS Catal.* **2020**, *10*, 1855–1864.
[55] Mavrikakis, M.; Hammer, B.; Nørskov, J. K. Effect of strain on the reactivity of metal surfaces. *Phys. Rev. Lett.* **1998**, *81*, 2819–2822.
[56] Stamenkovic, V.; Mun, B. S.; Mayrhofer, K. J. J.; Ross, P. N.; Markovic, N. M.; Rossmeisl, J.; Greeley, J.; Nørskov, J. K. Changing the activity of electrocatalysts for oxygen reduction by tuning the surface electronic structure. *Angew. Chem., Int. Ed.* **2006**, *45*, 2897–2901.
[57] Chen, Z. Y.; Song, Y.; Cai, J. Y.; Zheng, X. S.; Han, D. D.; Wu, Y. S.; Zang, Y. P.; Niu, S. W.; Liu, Y.; Zhu, J. F. et al. Tailoring the d-band centers enables Co_4N nanosheets to be highly active for hydrogen evolution catalysis. *Angew. Chem., Int. Ed.* **2018**, *57*, 5076–5080.

This is an open access article under the terms of the Creative Commons Attribution 4.0 International License (CC BY 4.0, https://creativecommons.org/licenses/by/4.0/).

© The Author(s) 2025. Published by Tsinghua University Press.